



Quantum yield measurements by thermal lens in highly absorbing samples: The case of highly doped rhodamine B organic/silica xerogels

J. F. M. dos Santos, V. S. Zanuto ^{*}, M. Ventura, C. B. Bramorski, and T. Catunda
Instituto de Física de São Carlos, Universidade de São Paulo, São Carlos, SP 13566-590, Brazil

D. S. Manoel
Instituto de Física de São Carlos, Universidade de São Paulo, São Carlos, SP 13566-590, Brazil
and Departamento de Física, Universidade Estadual Paulista, UNESP, Rio Claro, SP 13506-900, Brazil

L. C. Malacarne
Departamento de Física, Universidade Estadual de Maringá, Maringá, PR 87020-900, Brazil

F. S. de Vicente
Departamento de Física, Universidade Estadual Paulista, UNESP, Rio Claro, SP 13506-900, Brazil

 (Received 27 June 2019; revised manuscript received 1 October 2019; published 4 November 2019)

In this work, rhodamine B-doped GPTS/TEOS-derived organic/silica monolithic xerogels were prepared by the predoping sol-gel process. Thermal lens method was applied to determine thermo-optical properties of the samples. Since the samples present a high optical absorption coefficient, the high absorption theoretical TL model was introduced. Thermal diffusivities, optical absorption coefficients, and fluorescence quantum yield values were determined for samples with different rhodamine B (RhB) concentrations, from 10^{-5} to 10^{-2} M. The dye-doped organic/silica xerogels present a high fluorescence quantum yield (up to 90%), maintaining the value over 50% until a concentration of ~ 1.6 mM. To the best of our knowledge, RhB-doped transparent monoliths with a high fluorescence quantum yield with the highest RhB concentration reported in a solid hybrid matrix were obtained.

DOI: [10.1103/PhysRevMaterials.3.115201](https://doi.org/10.1103/PhysRevMaterials.3.115201)

I. INTRODUCTION

The study of modern photonic materials based on laser dyes incorporated in organic-inorganic hybrid hosts is an area of wide technological interest [1–3]. Numerous applications are given to these materials such as solid-state dye lasers [4–8], organic LEDs [9,10], dye-based optical chemical and biological sensors [11,12], and solar concentrators [13–15]. Researches conducted over the last few decades have been focused on new organic/inorganic hybrid materials, as sol-gel derived organic/silica materials [15–17]. These materials can combine the advantages of inorganic components with those of organic polymers, in which it is possible to obtain high optical quality, chemical stability, considerable mechanical strength, and other properties associated with the interaction of the individual organic and inorganic constituents [17]. The use of synthetic polymers as hosts still presents additional advantages, as these materials show a better compatibility with organic dyes like xanthenes [3,18].

In order to maximize the brightness, high dye-dopant concentrations are desirable. However, the molecular aggregation (formation of dimers, trimers, etc.) leads to the reduction of fluorescence quantum efficiency (η), or also denominated as

quantum yield, with the increase of dye concentration both in liquids and solids. This quenching effect is usually explained by the formation of fluorescent and nonfluorescent dimers (J and H dimers, respectively) in the concentration range 0.1–1 mM [5–7]. This process is critically dependent on host-guest interaction and it is expected that the incorporation of dyes into solid matrices can improve η due to the reduction of aggregation effects.

The absolute value of η is one of the most important properties for comparing fluorophores and luminescent materials. The η of transparent materials, such as solutions of molecular fluorophores, are usually determined with optical photometric techniques, which can be absolute or relative. The relative methods compare the integral sample emission and a fluorescent standard with a known η , under identical measurement conditions. The absolute method uses integrating sphere setups which, in principle, need no standard materials [19]. However, the determination of the absolute value of η for nontransparent solid samples has been shown to be a difficult task, due to signal/noise ratio or sample geometry. Hereupon, several photothermal techniques have been used to measure η of solid and liquid materials [20–24], since they provide the nonradiative quantum efficiency. Among these methods, several variations of the thermal lens (TL) method were used in luminescent materials [25–30], including quantum dots embedded in sol-gel glasses [17].

^{*}vszanuto@gmail.com

The conventional TL theory assumes an infinite sample, both in radial and axial directions, in which only radial heat flow is considered, so it is a two-dimensional (2D) model. In principle, this model is not suitable for highly absorbing samples ($A_e L > 1$) such as found in dyes incorporated in a solid matrix, where $A_e > 10^3 \text{ cm}^{-1}$ is obtained for concentrations in the millimolar range. In this case, the heat profile penetrates the sample deeper than the strongly attenuated excitation beam, so the axial heat flow should be taken into account.

In this paper, a 3D theoretical model for TL was developed in order to analyze data of highly absorbing samples and evaluate the fluorescence quantum efficiency. Rhodamine B (RhB)-doped GPTS/TEOS-derived organic/silica monolithic xerogels were prepared by the sol-gel method. The effect of concentration quenching on η was investigated in the concentration range from 0.036 to 19.4 mM. Waveguides fabricated by femtosecond laser writing technique were previously observed on these materials [31] as well as random laser (in highly doped bulk samples, $\approx 20 \text{ mM}$) [3]. As expected, $\eta \rightarrow 1$ in very diluted samples and decreases monotonically with an increase of dye concentration. Defining the critical quenching concentration Q as the concentration for η decreases to $\approx 50\%$, we obtained $Q \approx 1.6 \text{ mM}$ in xerogels. This value is 7 times higher than the highest value obtained for RhB diluted in an alcoholic solution [32].

II. EXPERIMENT

Hybrid organic/silica monolithic xerogels doped with RhB were obtained by the sol-gel process [3], using as precursors the alkoxides 3-glycidoxypropyltrimethoxysilane (GPTS) and tetraethylorthosilicate (TEOS) dissolved in ethanol (EtOH). The samples were prepared by acid hydrolysis, dropping a solution of HNO_3 (0.6 M in water) into the GPTS/TEOS/EtOH mixture, with a molar ratio of 1:1:3:4:0.1 for GPTS:TEOS:EtOH:H₂O:HNO₃, respectively. This process stays under mechanical stirring and reflux for 24 h with a controlled temperature of 80 °C. After the hydrolysis, the hybrid organic/silica sol is finished with a 1:1 GPTS/TEOS ratio. Solutions of RhB (Sigma-Aldrich) were prepared in EtOH with concentrations ranging from 0.05 to 25 mM. In the following step, the sols were doped with the RhB solutions in the ratio of 4:1. Bulks of RhB-doped xerogels were obtained after a controlled drying process at 40 °C. The final RhB concentrations in the solids were determined by density measurements, which are 0.036, 0.096, 0.193, 0.386, 1.94, 3.86, 4.825, 6.56, 9.65, and 19.4 mM, or in weight ratio: 0.012, 0.033, 0.067, 0.13, 0.67, 1.32, 1.65, 2.24, 3.29, and 6.57 wt. %, respectively.

These xerogels showed excellent optical quality, free of cracks, and present no porosity when measured by nitrogen adsorption [3]. The samples were prepared for optical measurements and presented thickness, in general, close to $L = 1 \text{ mm}$. The VIS absorption and emission spectra were measured in a Varian Cary 50 spectrophotometer and in a Varian Cary Eclipse fluorescence spectrophotometer, respectively. Representative absorption spectra of the samples are shown in Fig. 1. The inset shows the linear behavior of an

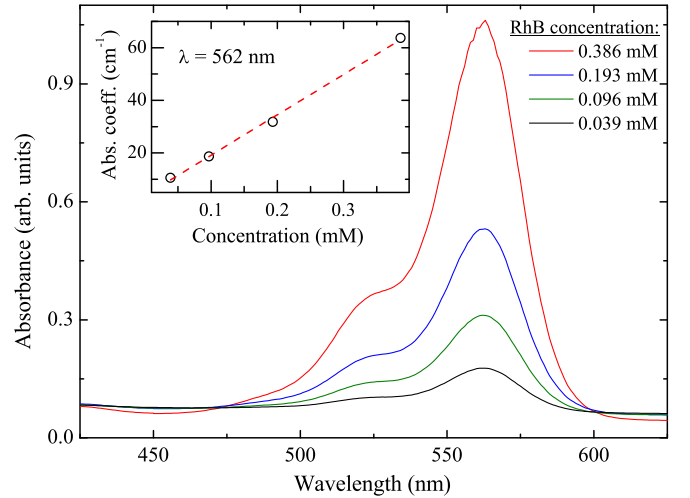


FIG. 1. Absorbance of RhB-doped GPTS/TEOS xerogels. Inset shows the linear behavior of an absorption coefficient at 562 nm with the RhB concentration.

absorption coefficient with RhB concentration, indicating a successful incorporation of the dye in the xerogel matrix.

The fluorescence quantum efficiencies of the samples were determined using a dual-beam pump-probe TL experiment. The TL effect takes place when a laser beam (excitation beam) passes through an absorbing medium. Absorbed energy followed by nonradiative processes induces a temperature increase, which causes thermal expansion and a refractive index gradient in the medium. These medium responses change the wavefront curvature of a second laser beam (probe beam) at a nonabsorbing wavelength. Thus, the sample acts like a lens, focusing or defocusing the probe beam. The TL experiment was performed using the conventional time-resolved dual-beam mode-mismatched configuration [29]. A green He-Ne laser ($\lambda_e = 543 \text{ nm}$) was used as the excitation beam and a red He-Ne laser ($\lambda_p = 632.8 \text{ nm}$) as the probe beam for the TL effect. The radii at the sample were $w_e = 55 \mu\text{m}$ and $w_p = 195 \mu\text{m}$ for the excitation and probe beams, respectively. As shown in Fig. 1, the samples are strongly absorbing at λ_e and transparent at λ_p . The excitation incidence was modulated with a chopper operating at $\approx 5 \text{ Hz}$ to ensure enough time to induce the TL effect in the gain medium and to observe the system reaching steady state. The temporal evolution of the on-axis probe beam intensity $I(t)$ was measured in the far field. Figure 2 shows three typical normalized TL transient signals for the xerogel samples doped with 0.036 and 19.4 mM of RhB, obtained with different excitation powers (P_e).

III. THEORY

The temperature change distribution inside an isotropic material $T(r, z, t)$ is described by the solution of the heat-conduction differential equation [26]

$$\frac{\partial}{\partial t} T(r, z, t) - D \nabla^2 T(r, z, t) = Q(r, z, t), \quad (1)$$

where D is the thermal diffusivity of the material and $Q(r, z, t)$ is a source term, which depends on the type of excitation. Time dependency can be addressed to continuous-wave or

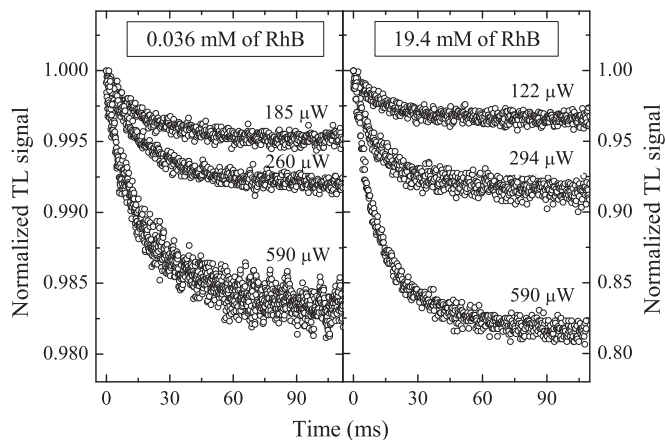


FIG. 2. Experimental TL signals for two different RhB concentrations, 0.036 and 19.4 mM, in different excitation powers.

pulsed laser. The spatial dependency is related to the spatial energy distribution of the laser beam, such as Gaussian or top-hat distributions. Besides that, the source term depends on the sample capacity to absorb photon energy and to convert into thermal energy.

Since in this paper a continuous-wave Gaussian profile excitation beam is used, the source term is written as $Q(r, z) = Q_0 e^{-2r^2/w_e^2} e^{-A_e z}$, where the azimuthal dependency is due to the Beer-Lambert law. $Q_0 = 2P_e A_e \phi / (\rho c_p \pi w_e)$, where A_e , ρ , and c_p are the optical absorption coefficient, density, and specific heat of the material, respectively. P_e and w_e are the incident power and the radius of the excitation beam, respectively. ϕ is the fraction of absorbed energy converted to heat, also denominated as nonradiative quantum efficiency. A full analytical model is not available for the finite sample considering the appropriate boundary conditions. However, it is viable to consider a sample with radial dimension larger than the excitation beam waist, and also to consider that heat does not spread to the sample radial boundary, in the case of short transients (milliseconds). In this case, the approximation of an infinite radial sample can be used. In addition, when the thermal conductivity of the surrounding fluid is much lower than the sample, the approximation of null heat flux to the surrounding fluid can be considered [33]. Then, the solution of the thermal diffusion equation can be obtained using the Laplace and Hankel transforms, leading to the temperature in Laplace-Hankel space [33], $T(\alpha, z, s)$, which is a function of the spatial frequency (α) and temporal frequency (s) coordinates,

$$(s + D\alpha^2)T(\alpha, z, s) - D \frac{\partial^2}{\partial z^2} T(\alpha, z, s) = Q_0 \frac{w_e^2}{4s} e^{-\frac{1}{8} w_e^2 \alpha^2} e^{-A_e z}. \quad (2)$$

The solution of this differential equation with the null heat flux condition at the surfaces ($z = 0, L$) can be obtained easily, whereas the inversion of the Laplace and Hankel transforms become hard to perform. A special case in which the inversion of these transforms are possible is the very low optical absorption condition ($A_e L < 0.1$). In this approximation, the temperature is almost constant along the axial (z) direction, so $T(r, z, t) \approx T(r, t)$. Consequently, heat diffusion occurs only in the radial direction, so-called 2D model, and the

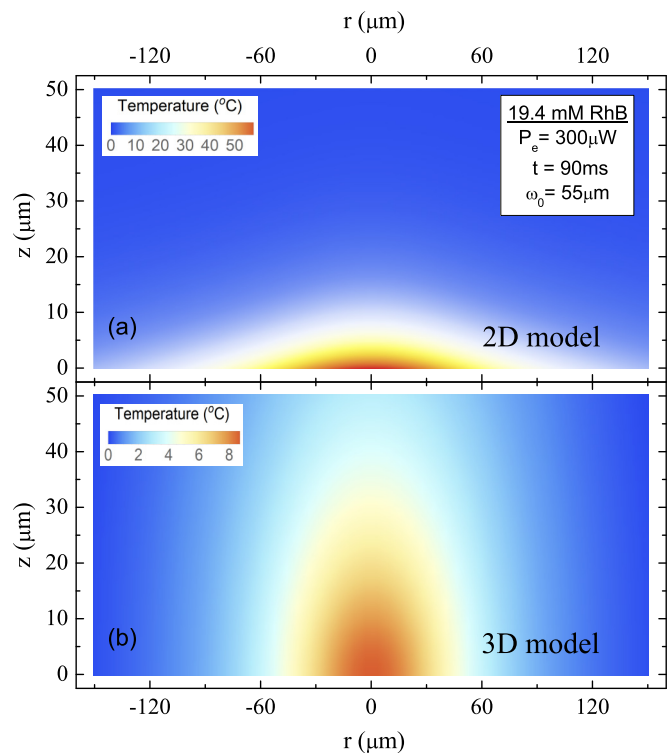


FIG. 3. Temperature distribution in a section of the sample doped with 19.4 mM, considering (a) the 2D model corrected by the attenuation factor, and (b) the 3D model numerically solved.

temperature change is given by [34]

$$T(r, t) = \frac{2P_e A_e \phi}{\pi \rho c_p} \int_0^t \frac{\exp\left(-\frac{2r^2/w_e^2}{1+2\tau/t_c}\right)}{w_e^2(1+2\tau/t_c)} d\tau, \quad (3)$$

where $t_c = w_e^2/4D$ is the characteristic TL signal response time.

Although these considerations are valid approximations in many important cases, for high absorption materials ($A_e L > 1$), the attenuation of the beam energy along the axial direction induces diffusion in both radial and axial directions, making it necessary to be taken into account. A first attempt to overcome this limitation is to refine the temperature of the 2D model with the direct inclusion of the attenuation factor, as $T(r, z, t) \approx e^{-A_e z} T(r, t)$ [27], however, this correction must be examined.

Figure 3 presents a comparison between the temperature density maps calculated using the 2D model corrected by the attenuation factor $e^{-A_e z}$ and the complete 3D model in the quasistationary state ($t \approx 19t_c = 90$ ms). Equation (2) was solved numerically using *Wolfram Mathematica 7.1* to obtain the temperature maps shown in Fig. 3, for the highly doped sample (19.4 mM of RhB) with $A_e = 1601 \text{ cm}^{-1}$ ($A_e L \approx 160$). In Fig. 3(a) the corrected 2D model predicts a significant temperature increase only at the surface, since the penetration length ($A_e^{-1} \approx 6 \mu\text{m}$) is much shorter than L . In Fig. 3(b) a complete different temperature density map is obtained with the 3D model, where both radial and axial heat diffusions are considered. In this case, the temperature increase at the center ($r = 0$) is lower than the 2D model by a 6.62 factor.

Moreover, the heat penetrates deeper ($\sim 55 \mu\text{m}$) inside the material. Therefore, Fig. 3 shows one relevant situation (to our experimental data), where the 2D model clearly fails to describe the temperature distribution. However, as expected, we verified that the 2D approximation converges to the 3D result for the low absorption case.

The phase shift induced in the probe beam $\Phi(r, t)$ is written in terms of the temperature change and, in the plane-stress approximation, is given by

$$\Phi(r, t) = \frac{2\pi}{\lambda_p} \frac{dS}{dT} \int_0^L [T(r, z, t) - T(0, z, t)] dz, \quad (4)$$

where λ_p is the probe beam wavelength and dS/T is the temperature coefficient of the optical path at the probe wavelength.

It is important to highlight that the knowledge of the full temperature profile $\Delta T(r, z, t)$ is not necessary to obtain the TL effect, but only $\Phi(r, t)$ given by the integral in Eq. (4). Therefore, a full analytical solution is achieved in the Laplace-Hankel space using the solution of Eq. (2) into Eq. (4),

$$\int_0^L T(\alpha, z, s) dz = Q_0 \frac{1 - e^{-A_e L}}{A_e} \frac{w_e^2 e^{-\frac{1}{8} w_e^2 \alpha^2}}{4s(s + D\alpha^2)}. \quad (5)$$

Thus, the inverse Laplace and Hankel transforms can be easily performed, and the phase shift reduces to

$$\begin{aligned} \Phi(r, t) = \frac{\theta_{\text{eff}}}{2} \left[-\text{Ei}\left(-\frac{2r^2}{w_e^2}\right) + \text{Ei}\left(-\frac{2r^2 t_c}{w_e^2(2t + t_c)}\right) \right. \\ \left. + \text{Log}\left(\frac{2t + t_c}{t_c}\right) \right], \quad (6) \end{aligned}$$

where $\text{Ei}(x)$ is the exponential integral function. Here θ_{eff} is defined by

$$\theta_{\text{eff}} = -\frac{P_e A_e}{k \lambda_p} \frac{dS}{dT} L_{\text{eff}} \phi, \quad (7)$$

where $k = D\rho c_p$ is the thermal conductivity of the sample, and the sample effective length is $L_{\text{eff}} = (1 - e^{-A_e L})/A_e$.

Finally, after its passage through the sample, the probe beam profile can be calculated in the far field using the Fresnel-Kirchhoff diffraction integral. For the TL calculation, the interest is only in the central portion of the probe beam intensity change ($r = 0$). In the case of radial symmetry, it is convenient to use the change of variable $g = (r/w_p)^2$, where w_p is the probe beam radius in the sample, in order to obtain [33]

$$\frac{I(t)}{I(0)} = (1 + V^2) \left| \int_0^\infty \exp[-(1 + iV)g - i\Phi(g, t)] dg \right|^2, \quad (8)$$

where $I(0)$ is the intensity when $t = 0$ and $V = Z_1/Z_c + Z_c[1 + (Z_1/Z_c)^2]/Z_2$ is an experimental parameter [29], Z_c is the confocal distance of the probe beam, Z_1 is the distance between the sample and the probe beam waist, and Z_2 is the distance between the sample and the detector plane.

In general, the intensity $I(t)$ in Eq. (8) should be numerically calculated. However, for small phase shift (θ_{eff} or $\Phi \ll 1$), the approximation $e^{i\Phi} \simeq 1 - i\Phi$ is applicable, allowing a

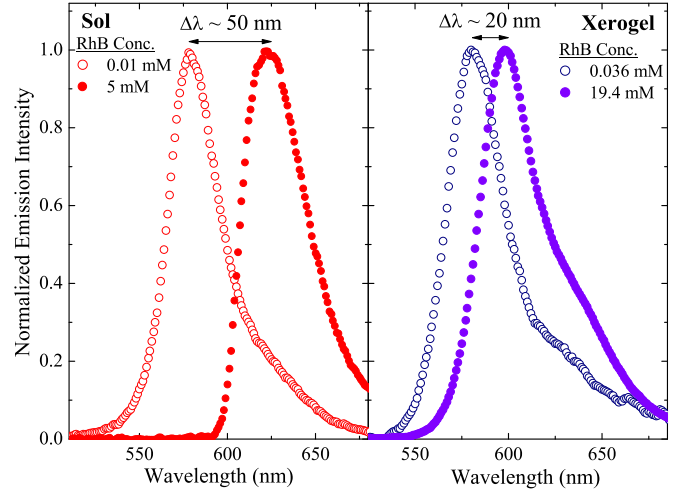


FIG. 4. Emission spectra of RhB-doped GPTS/TEOS sol and xerogels with lowest (open circles) and highest (solid circles) RhB concentrations. Redshift occurs for higher concentrations.

simple analytical solution,

$$\begin{aligned} \frac{I(t)}{I(0)} \\ = \left[1 - \frac{\theta_{\text{eff}}}{2} \tan^{-1} \left(\frac{2mV}{[(1 + 2m)^2 + V^2] \frac{t_c}{2t} + 1 + 2m + V^2} \right) \right]^2, \quad (9) \end{aligned}$$

where $m = (w_p/w_e)^2$ is the ratio between the radii of probe and excitation beams in the sample [29]. Equation (9) shows that the TL signal amplitude is proportional to the parameter θ_{eff} which is proportional to the heat power delivered into the sample, so it is proportional to the product of absorbed excitation power ($P_e A_e L_{\text{eff}}$) and the nonradiative quantum efficiency of the sample (ϕ). The parameter ϕ will be used to determine η , as discussed later in this paper.

It is remarkable that Eq. (9) is the same expression previously obtained with the 2D model with just the replacement of L_{eff} by L , where θ_{eff} became equivalent to θ of Ref. [34]. We remind that $L_{\text{eff}} \rightarrow L$ when $A_e L \rightarrow 0$. However, it is not obvious that the 2D approximation $T(r, z, t) \approx e^{-A_e z} T(r, t)$ results in the same $\Phi(r, t)$ profile as the 3D model, since their temperature change distributions are quite different, as shown in Fig. 3. This means that the phase profile, as defined by the integral of Eq. (2), is not affected by heat diffusion along z direction.

IV. RESULTS AND DISCUSSION

Figure 4 compares emission spectra of RhB-doped organic/silica sol and xerogel samples, with the lowest and highest RhB concentrations. The peak emission shifts to the red with the concentration increase from 0.036 to 19.49 mM. In the case of sol samples, the redshift was $\Delta\lambda \sim 50 \text{ nm}$. This redshift is higher than observed in the corresponding xerogel samples, $\Delta\lambda \approx 20 \text{ nm}$. The redshift can be attributed to aggregation and rotational relaxation modes, leading to energy

loss by the nonradiative process [7]. In the liquid matrix, RhB molecules should exhibit more rotational modes, leading to higher energy loss and resulting in a larger shift. In the xerogel matrix, the dye translational freedom is suppressed, and intermolecular collisions prevented [16]. Since the rotational relaxation of the excited state of laser dyes is one of the main modes of nonradiative energy losses, the xerogel matrix reduces the internal rotational modes, reducing the energy loss and increasing the fluorescence quantum yield [35]. Thus, aggregational and translational collisions that stimulate the deactivation process of the laser dye are prevented.

The basic idea of an all photothermal method is that the signal is proportional to the fraction of absorbed energy converted to heat (ϕ), so for η measurements, it is considered that $\phi = (1 - \eta\lambda_e/\langle\lambda_{em}\rangle)$, where $\langle\lambda_{em}\rangle$ is the mean emission wavelength [27]. By TL results, Eq. (7) gives access to the η . In principle, the parameter $k^{-1}dS/dT$ of Eq. (7) should be known in order to determine η from the TL data. Nevertheless, this parameter can be determined using a reference sample, given by the same host matrix but doped with a nonfluorescent dye ($\eta = 0$, then $\phi = 1$). For this purpose, a red ink (Disperse Red 19 Sigma-Aldrich)-doped GTPS/TEOS matrix was prepared using the same procedure as the RhB-doped samples, in order to use it as a reference standard. Therefore, normalizing the results of RhB-doped samples by the reference result, we obtain the sample quantum yields

$$\phi_{\text{sample}} = \frac{[\theta_{\text{eff}}/P_{\text{abs}}]_{\text{sample}}}{[\theta_{\text{eff}}/P_{\text{abs}}]_{\text{ref}}} = \left(1 - \eta \frac{\lambda_e}{\langle\lambda_{em}\rangle}\right). \quad (10)$$

As pointed out before, due to the redshift with the concentration, each sample presented a different value of $\langle\lambda_{em}\rangle$. Using these values and the θ_{eff} values obtained by theoretical fitting, the fluorescence quantum yield for RhB-doped xerogels were calculated. For instance, using the definition of θ (2D model [34]) or θ_{eff} (3D model), the 0.036 mM doped sample presented close values, such as $\phi = (0.15 \pm 0.01)$ and $\eta = (0.90 \pm 0.01)$. Figure 5 shows the discrepancy between the nonradiative quantum efficiencies (ϕ) obtained from 2D and 3D models increases with the concentration. In the case of the highest concentration (19.4 mM), using the definition of θ resulted in the unrealistic value $\eta = (1.09 \pm 0.01)$, while using the definition of θ_{eff} results in $\eta = (0.09 \pm 0.01)$.

As expected, η decreases with concentration, as presented in Fig. 6. This behavior can be described by a power-law expression,

$$\eta = \frac{\eta_0}{1 + (C/Q)^p}, \quad (11)$$

where η_0 represents the quantum efficiency in zero concentration limit or maximum molecular separation, Q is a critical concentration parameter ($\eta = \eta_0/2$ for $C = Q$), and the p indicates the type of intramolecular interaction. For instance, $p = 2$ is expected for Förster energy transfer rate (interaction with R^{-6} dependence). The fit of our experimental data results in $\eta_0 = (0.93 \pm 0.08)$, $p = (0.77 \pm 0.15)$, and $Q = (1.6 \pm 0.6)$ mM. The $Q \approx 1.6$ mM is nearly 7 times higher than found in solutions of RhB in methanol by Bindhu *et al.* [32]. Our Q value is also higher than observed in most of Rh6G-doped silica hybrids with Q typically lower than 10^{-4} M [7,18]. The small p value obtained is also a desirable

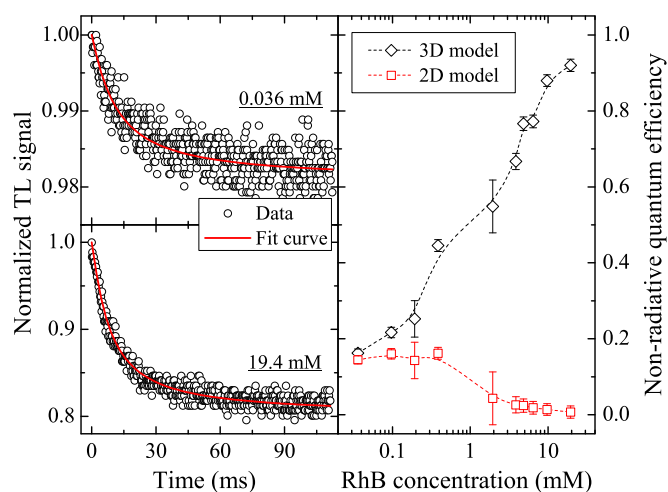


FIG. 5. On the left: Experimental TL signals (circles) of two samples, doped with 0.036 mM (up) and 19.4 mM (down) of RhB, for excitation power $P_e = 590 \mu\text{W}$. Red line corresponds to the fitting curve using Eq. (8). On the right: Nonradiative quantum efficiency (ϕ) obtained from fitting results using the 2D model (squares) and 3D model (diamonds), dashed lines are a guide for the eyes.

feature indicating a gradual transition to the formation of nonfluorescent aggregates. This $p \approx 0.77$ value is equivalent to $R^{-2.3}$ dependence in agreement with the results obtained by Green and Buckley for Rh6G in PMMA [13]. This behavior might indicate the role of surface-surface interaction with a R^{-2} dependence [36]. In fact, in Ref. [13], seven different dyes were investigated and the p values varied between 0.8 and 1.4.

In the literature it is well known that dye molecules may have mobility in the sol-gel matrix allowing molecular aggregation or sample bleaching [2,5–7]. This behavior is observed mainly in materials synthesized by simple mixing in a common solvent of the mineral precursor prior to

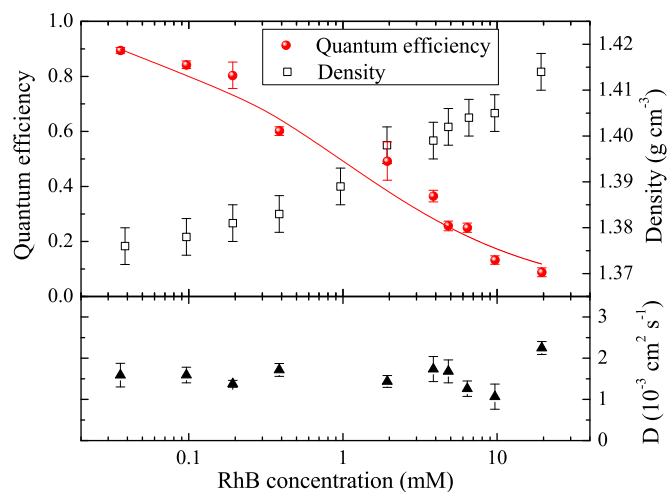


FIG. 6. Quantum efficiency η (solid circles), thermal diffusivity D (solid triangles), and density (open squares) for RhB-doped GTPS/TEOS xerogels. Red line is the fit curve using Eq. (11).

hydrolysis with organic molecules or macromolecules (hybrids class I). In this way, numerous materials have been prepared embedding organic dyes or optically active molecules, called post-doping method [2]. However, organic molecules are physically trapped into the silica matrix by electrostatic interactions. On the other hand, the predoping method used in this work is preferred since it allows the reduction or elimination of leaching drawbacks typical of impregnation (class II-hybrid materials). In this case, the dye molecules are covalently bonded to the organic moiety of the organic/silica matrix due to the functional groups of organosilane alkoxide, as the case of GPTS alkoxide. The opening of epoxy groups from GPTS promotes the covalent bond of organic dyes into the matrix [2,5–7] and a large amount of dye can be incorporated avoiding fluorescence quenching due to dye aggregation.

The gradual quantum efficiency decrease even at high concentrations of RhB favors the application of this material for solar concentrators [13–15] and lasers [7,8]. Besides the samples being class II-hybrid materials, another characteristic of this material which may contribute to the high η values is the lack of porosity, mentioned in the sample preparation section [3]. Few papers on hybrid materials have reported physical properties improvement due to the absence of porosity. Jain *et al.* [37] analyzed thermal properties of silica matrix, like polymeric and xerogel films. They observed that in the absence of any impurity, microcracks and microporosity, the sintered silica presented the highest thermal conductivity compared to the other studied materials. They claim that the presence of impurities or microporosity leads to increased nonradiative decay processes (phonon scattering). In addition to them, Arachchige *et al.* [38] have reported large optical changes attributed to densification of the host network, due to physical bonds as well as the quality of the interface between the particles. We also remind that solid matrices usually prevent large redshifts in fluorescent spectra, at higher dye concentrations, indicating less energy loss by nonradiative processes, as molecular rotation or vibrations [7]. However, further studies are needed to verify directly the relation between the matrix porosity and the fluorescence quenching mechanisms.

Figure 6 also shows the behavior of the sample thermal diffusivity (D), which is nearly constant (within $\pm 8\%$) up to 6 mM. Although the density increases with RhB

concentration, this increase is very small ($< 2\%$) and does not affect D . The mean value for D is $1.56 \times 10^{-3} \text{ cm}^2 \text{ s}^{-1}$, which is similar to values already reported for similar materials [39]. High values of thermal diffusivity are desirable for solid-state laser systems.

V. CONCLUSION

In summary, efficient fluorescent rhodamine B-doped GPTS/TEOS-derived organic/silica monolithic xerogels were obtained by the predoping sol-gel method. The solid xerogels presented advantages compared to sol medium, due to the diminishing of redshift in the RhB emission. The redshift indicates energy losses by nonradiative processes, as molecular rotation or vibration, which in solids are suppressed. The quantum efficiency (η) measured for the xerogel with lowest RhB concentration was $\approx 90\%$ and decreased to 9% for the sample with 19.4 mM. The η values agree with the redshift observed in the sample emission, for higher concentrations nonemissive molecular aggregates form more easily, leading to energy loss by a nonradiative process, decreasing the η value. These results are distinguished due to the values of quantum efficiency here reported, which are higher than others in the literature, even with the high RhB concentrations used in our samples. The higher value can be attributed to the predoping method, which obtains the type II hybrids, where the host and guest are bonded covalently, being more photostable than the electrostatic bonded type I hybrids. Besides that, the absence of porosity of the host material also may contribute to higher η values, however, more investigations are necessary. Ultimately, the access to quantum efficiency of these highly doped materials was possible due to the development of the high absorption theoretical thermal lens model (3D model), since the limitation of low absorption material approximation of the 2D model has been overcome in this work.

ACKNOWLEDGMENTS

The authors thank the Brazilian agencies: CNPq (M.V., Grant No. 150732/2017-1), CAPES, and FAPESP (V.S.Z., Grant No. 2017/16392-6) for the financial support of this work.

-
- [1] J. Clark and G. Lanzani, *Nat. Photonics* **4**, 438 (2010).
 - [2] B. Lebeau and P. Innocenzi, *Chem. Soc. Rev.* **40**, 886 (2011).
 - [3] L. M. G. Abegão, D. S. Manoel, A. J. G. Otuka, P. H. D. Ferreira, D. R. Vollet, D. A. Donatti, L. De Boni, C. R. Mendonça, F. S. De Vicente, J. J. Rodrigues, Jr., and M. A. R. C. Alencar, *Laser Phys. Lett.* **14**, 065801 (2017).
 - [4] C. M. Carbonaro, A. Anedda, S. Grandi, and A. Magistris, *J. Phys. Chem. B* **110**, 12932 (2006).
 - [5] S. Grandi, C. Tomasi, P. Mustarelli, F. Clemente, and C. M. Carbonaro, *J. Sol-Gel Sci. Technol.* **41**, 57 (2007).
 - [6] A. Anedda, C. M. Carbonaro, R. Corpino, P. C. Ricci, S. Grandi, and P. C. Mustarelli, *J. Non-Cryst. Solids* **353**, 481 (2007).
 - [7] C. M. Carbonaro, P. C. Ricci, S. Grandi, M. Marceddu, R. Corpino, M. Salis, and A. Anedda, *RSC Adv.* **2**, 1905 (2012).
 - [8] O. Mhibik, T. Leang, A. Siove, S. Forget, and S. Chénais, *Appl. Phys. Lett.* **102**, 041112 (2013).
 - [9] H. Nakanotani, T. Higuchi, T. Furukawa, K. Masui, K. Morimoto, M. Numata, H. Tanaka, Y. Sagara, T. Yasuda, and C. Adachi, *Nat. Commun.* **5**, 4016 (2014).
 - [10] D. A. Moghe, A. Dey, K. Johnson, L.-P. Lu, R. H. Friend, and D. Kabra, *Appl. Phys. Lett.* **112**, 163301 (2018).
 - [11] B. Choudhury, R. Shimar, and J. Shinar, *J. Appl. Phys.* **96**, 2949 (2004).

- [12] S. Mehrabani, A. J. Maker, and A. M. Armani, *Sensors* **14**, 5890 (2014).
- [13] A. P. Green and A. R. Buckley, *Phys. Chem. Chem. Phys.* **17**, 1435 (2015).
- [14] S. F. Daorta, A. Proto, R. Fusco, L. C. Andreani, and M. Liscidini, *Appl. Phys. Lett.* **104**, 153901 (2014).
- [15] R. Rondão, A. R. Frias, S. F. H. Correia, L. Fu, V. Z. Bermudez, P. S. André, R. A. S. Ferreira, and L. D. Carlos, *ACS Appl. Mater. Interfaces* **9**, 12540 (2017).
- [16] T. Seckin, A. Gulteka, and S. Kartaca, *Dyes Pigments* **56**, 51 (2003).
- [17] L. D. S. Alencar, V. Pilla, A. A. Andrade, D. A. Donatti, D. R. Vollet, and F. S. de Vicente, *Chem. Phys. Lett.* **599**, 63 (2014).
- [18] T. B. Queiroz, M. B. S. Botelho, L. De Boni, H. Eckert, and A. S. S. de Camargo, *J. Appl. Phys.* **113**, 113508 (2013).
- [19] C. Würth, M. Grabbolle, J. Pauli, M. Spieles, and U. Resch-Genger, *Nat. Protocols* **8**, 1535 (2013).
- [20] J. H. Brannon and D. Magde, *J. Phys. Chem.* **82**, 705 (1978).
- [21] S. E. Braslavsky and G. E. Heibel, *Chem. Rev.* **92**, 1381 (1992).
- [22] J. A. Muñoz, J. O. Tocho, and F. Cussó, *Europhys. Lett.* **43**, 159 (1998).
- [23] Y.-F. Huang, H.-L. Chen, J. W. Ting, C.-S. Liao, R. W. Larsen, and W. Fann, *J. Phys. Chem. B* **108**, 9619 (2004).
- [24] B. Couch, A. Meyer, B. Heller, and S. L. Johnson, *Methods Appl. Fluoresc.* **7**, 015004 (2019).
- [25] M. L. Lesiecki and J. M. Drake, *Appl. Opt.* **21**, 557 (1982).
- [26] M. L. Baesso, A. C. Bento, A. A. Andrade, J. A. Sampaio, E. Pecoraro, L. A. O. Nunes, T. Catunda, and S. Gama, *Phys. Rev. B* **57**, 10545 (1998).
- [27] S. M. Lima, A. S. S. de Camargo, L. A. O. Nunes, T. Catunda, and D. W. Hewak, *Appl. Phys. Lett.* **81**, 589 (2002).
- [28] A. Santhi, M. Umadevi, V. Ramakrishnan, P. Radhakrishnan, and V. P. N. Nampoori, *Spectrochim. Acta A* **60**, 1077 (2004).
- [29] C. Jacinto, D. N. Messias, A. A. Andrade, S. M. Lima, M. L. Baesso, and T. Catunda, *J. Non-Cryst. Solids* **352**, 3582 (2006).
- [30] B. Pathrose, V. P. N. Nampoori, P. Radhakrishnan, H. Sahira, and A. Mujeeb, *J. Fluoresc.* **25**, 739 (2015).
- [31] P. H. D. Ferreira, A. J. G. Otuka, E. C. Barbano, D. S. Manoel, F. S. de Vicente, D. R. Vollet, D. A. Donatti, L. Misoguti, and C. R. Mendonça, *Opt. Mater.* **47**, 310 (2015).
- [32] C. V. Bindhu and S. S. Harilal, *Anal. Sci.* **17**, 141 (2001).
- [33] L. C. Malacarne, N. G. C. Astrath, G. V. B. Lukasiewicz, E. K. Lenzi, M. L. Baesso, and S. E. Bialkowski, *Appl. Spectrosc.* **65**, 99 (2011).
- [34] M. L. Baesso, J. Shen, and R. D. Snook, *J. Appl. Phys.* **75**, 3732 (1994).
- [35] M. A. Meneses-Nava, O. Barbosa-García, L. A. Díaz-Torres, S. Chávez-Cerda, M. Torres-Cisneros and, and T. A. King, *Opt. Mater.* **17**, 415 (2001).
- [36] J. Hill, S. Y. Heriot, O. Worsfold, T. H. Richardson, A. M. Fox, and D. D. C. Bradley, *Phys. Rev. B* **69**, 041303(R) (2004).
- [37] A. Jain, S. Rogojevic, S. Ponoth, W. N. Gill, J. L. Plawsky, E. Simonyi, S.-T. Chen, and P. S. Ho, *J. Appl. Phys.* **91**, 3275 (2002).
- [38] I. U. Arachchige, J. L. Mohanan, and S. L. Brock, *Chem. Mater.* **17**, 6644 (2005).
- [39] J. John, L. Thomas, A. Kurian, V. P. N. Nampoori, and S. D. George, *Microporous Mesoporous Mater.* **244**, 171 (2017).